Stankiewicz, J., Muñoz, G., Ritter, O., Bedrosian, P., Ryberg, T., Weckmann, U., Weber, M., DESERT GROUP (2011): Shallow lithological structure across the Dead Sea Transform derived from geophysical experiments. - Geochemistry Geophysics Geosystems (G3), Vol. 12, Q07019

DOI: 10.1029/2011GC003678

Geochemistry Geophysics Geosystems G3

Article
Volume 12, Number 7
23 July 2011
Q07019, doi:10.1029/2011GC003678
ISSN: 1525-2027

Published by AGU and the Geochemical Society

Shallow lithological structure across the Dead Sea Transform derived from geophysical experiments

J. Stankiewicz, G. Muñoz, and O. Ritter
Deutsches GeoForschungsZentrum, Telegrafenberg, D-14473 Potsdam, Germany (jacek@gfz-potsdam.de)

P. A. Bedrosian
U.S. Geological Survey, P.O. Box 25046, MS 150, Denver, Colorado 80225, USA

T. Ryberg and U. Weckmann
Deutsches GeoForschungsZentrum, Telegrafenberg, D-14473 Potsdam, Germany

M. Weber
Deutsches GeoForschungsZentrum, Telegrafenberg, D-14473 Potsdam, Germany

Institute for Geosciences, University of Potsdam, Potsdam, Germany

[1] In the framework of the DEad SEa Rift Transect (DESERT) project a 150 km magnetotelluric profile consisting of 154 sites was carried out across the Dead Sea Transform. The resistivity model presented shows conductive structures in the western section of the study area terminating abruptly at the Arava Fault. For a more detailed analysis we performed a joint interpretation of the resistivity model with a P wave velocity model from a partially coincident seismic experiment. The technique used is a statistical correlation of resistivity and velocity values in parameter space. Regions of high probability of a coexisting pair of values for the two parameters are mapped back into the spatial domain, illustrating the geographical location of lithological classes. In this study, four regions of enhanced probability have been identified, and are remapped as four lithological classes. This technique confirms the Arava Fault marks the boundary of a highly conductive lithological class down to a depth of ~3 km. That the fault acts as an impermeable barrier to fluid flow is unusual for large fault zone, which often exhibit a fault zone characterized by high conductivity and low seismic velocity. At greater depths it is possible to resolve the Precambrian basement into two classes characterized by vastly different resistivity values but similar seismic velocities. The boundary between these classes is approximately coincident with the Al Quweira Fault, with higher resistivities observed east of the fault. This is interpreted as evidence for the original deformation along the DST originally taking place at the Al Quweira Fault, before being shifted to the Arava Fault.

Components: 8000 words, 8 figures.

Keywords: magnetotellurics; seismic tomography.

Index Terms: 6982 Radio Science: Tomography and imaging (7270, 8180).

Received 28 April 2011; **Revised** 7 June 2011; **Accepted** 8 June 2011; **Published** 23 July 2011.

Stankiewicz, J., G. Muñoz, O. Ritter, P. A. Bedrosian, T. Ryberg, U. Weckmann, and M. Weber (2011), Shallow lithological structure across the Dead Sea Transform derived from geophysical experiments, *Geochem. Geophys. Geosyst.*, *12*, Q07019, doi:10.1029/2011GC003678.

1. Introduction

[2] The Dead Sea Transform (DST), separating the Arabian and African plates, is one the world's major transform faults (Figure 1). It extends over ~1000 km from the Red Sea Rift to the Taurus-Zagros collision zone. It has experienced 105 km of lateral displacement since 18 Ma [*Quennell*, 1958], though more recent studies suggest the displacement started at 15 Ma or earlier [*ten Brink et al.*, 1993; *Garfunkel and Ben-Avraham*, 1996]. The recent relative plate motion being 3–5 mm per year [*Klinger et al.*, 2000]. Between the Gulf of Aquaba and the Dead Sea the sinistral strike-slip Arava/Araba Fault (AF) constitutes the major branch of the DST [*Garfunkel et al.*, 1981]. One of the most prominent structures east of the AF is the Al Quweira Fault zone (AQF), considered to be a left-lateral fault [e.g., *Barjous and Mikbel*, 1990]. Horizontal displacement estimates along the AQF range from 8 km [*Abu Taimeh*, 1988] to up to 40 km [*Barjous*, 1988]. While a number of other faults have been mapped in the region, no indication of post-Miocene faulting has been found at any of them other than AF and AQF [*Ryberg et al.*, 2007].

[3] Fault zones are the locations where motion of tectonic plates, often associated with earthquakes, is accommodated. Since the advent of plate tectonics the DST has been considered a prime site to examine large shear zones. Large historical earthquakes on the DST with magnitudes up to 7 [e.g., *Garfunkel et al.*, 1981] as well as ongoing microseismic activity [e.g., *Aldersons et al.*, 2003] show that the DST is a seismically active plate boundary. In the framework of the international geoscientific DEad SEa Rift Transect (DESERT) project [*DESERT Group*, 2000; *Weber et al.*, 2004, 2009], a number of geophysical experiments have been carried out in the region of the DST. The central questions addressed in this project were (1) What are the structure and kinematics of a large fault zone? (2) What controls its structure and kinematics? (3) How does the DST compare to other transform plate boundary fault zones? The experiments carried out to address these questions included wide-angle seismic investigations [*Mechie et al.*, 2005], a near-vertical seismic experiment [*Ryberg et al.*, 2007], receiver function studies [*Mohsen et al.*, 2005, 2006], and magnetotelluric (MT) experiments [*Ritter et al.*, 2003]. Joint interpretations of some of these geophysical experiments have also been undertaken [e.g., *Maercklin et al.*, 2005; *Bedrosian et al.*, 2007]. This study presents the first comprehensive resistivity model computed from all the available MT data collected, and presents a lithological structure classification of the uppermost 5 km from a joint interpretation of this resistivity model with a coincident P wave velocity model [*Ryberg et al.*, 2007].

[4] The collected MT data were the first continuous profile in the area aimed to image the subsurface at kilometer scale. Previous electromagnetic experiments in the region dealt with individual MT sites [e.g., *Rotstein and Goldberg*, 1981], or used the transient electromagnetic method to provide detailed images of the uppermost ~100m [e.g., *Ezersky*, 2008; *Rödder*, 2010].

2. Magnetotelluric Surveys Across the Dead Sea Transform

2.1. Data Acquisition

[5] The magnetotelluric data were collected in three separate field campaigns (Figure 1). This technique uses natural electromagnetic field variations to estimate the subsurface resistivity structure. Resistivity is related to factors like fluid content, salinity, and mineralization. In 2000, 31 stations were deployed in a short (10 km) profile across the AF. The profile had a very dense site spacing of 100 m near the surface trace of the AF to increase resolution at the area of interest, with the stations becoming more widely spaced (1 km) near the profile ends. The profile was extended with 76 stations deployed in Jordan in 2002 with site spacing of 1–3 km, and 47 stations deployed in Israel in 2003 (site spacing 1–2 km) completing a 150 km profile. At each station the magnetic field variations were measured as a time series in the period range 0.001–1000 s in three orthogonal components using induction coil magnetometers, and the electric field variations in the two horizontal components using nonpolarizable electrodes.

[6] The data were processed using the technique of *Ritter et al.* [1998] and *Weckmann et al.* [2005] to obtain frequency dependent values for apparent resistivity, phase, and vertical magnetic field transfer functions (represented as induction arrows). The collected data were generally of high quality, however, in some regions, particularly on the Israeli side, stations were severely disturbed by cultural electromagnetic noise. Recent reprocessing including the application of the remote reference technique [*Gamble et al.*, 1979; *Krings*, 2007] greatly improved

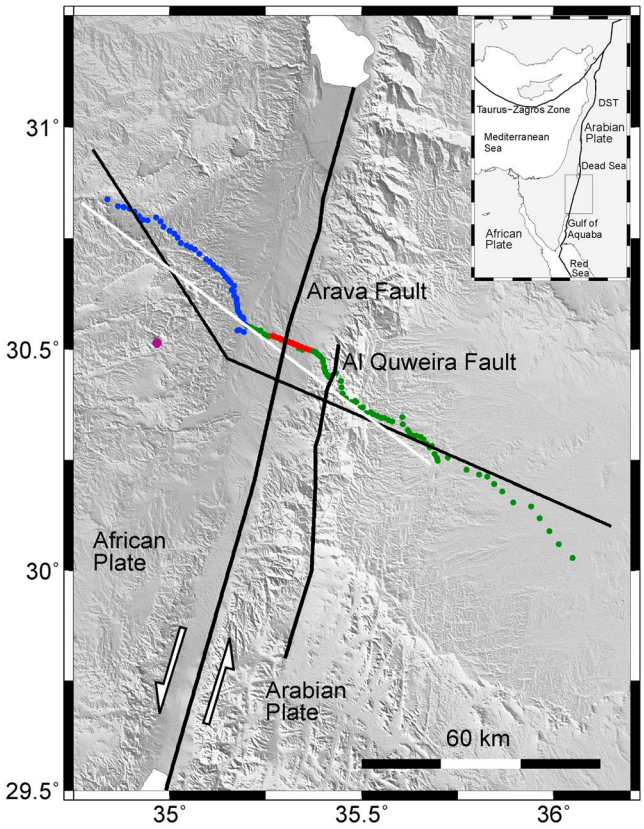

Figure 1. Location of the MT stations used in this study, deployed in three field campaigns. Thirty-one densely spaced stations deployed across the Arava Fault are marked in red, 76 stations from the campaign in Jordan are marked in green, and 47 stations from the Israel campaign are marked in blue. One station in Israel was only used for remote reference processing; it is marked in purple. The crooked black line shows the profile onto which the sites were projected. The orientation represents a compromise between the calculated strike direction and the geometry of site distribution. The white line shows the profile onto which the seismic experiment of *Ryberg et al.* [2007] was projected. Locations of the Arava (AF) and Al Quweira (AQF) Faults are shown. Arrows indicate the relative plate motion.

the results in the relevant region. An example is presented in Figure 2, which shows significant improvement in a period range from 1 to 20s.

2.2. Dimensionality Analysis

[7] The dimensionality of the data was analyzed using the algorithm of *Becken and Burkhardt* [2004]. This technique examines the polarization of the telluric vectors (columns of the impedance tensor), which in the general case is elliptical. If a coordinate system can be found where the telluric vectors are linearly polarized (i.e., the ellipticities vanish), the impedance tensor can be decomposed into a regional two-dimensional (2-D) tensor and a real distortion matrix. In practice such a coordinate system is sought by minimizing the sum of squared ellipticities over a range of periods and sites with respect to a rotation angle. This analysis carries a 90 degree ambiguity, which can be solved using the induction vectors (they should point perpendicular to the geoelectric strike) or known geological information. Figure 3a shows the rose diagram of the strike directions calculated for each available site using the entire period range. Clearly no dominant direction exists.

[8] A thorough investigation of the dependence of ellipticities on period yielded conditions under which a 2-D analysis of the data would be appropriate. It was found that in the period range 0.4–10 s, the 3-D effects are negligible, and strike directions well defined – albeit differently in two sections of the profile. Analyzing the strike distribution on a site by site basis, the profile was divided into two sections, for each of which a single, well-defined strike direction can be determined. These two sections correspond approximately with the profile segments located respectively in Israel and Jordan, i.e., the geoelectric strike changes at the border. Figures 3b

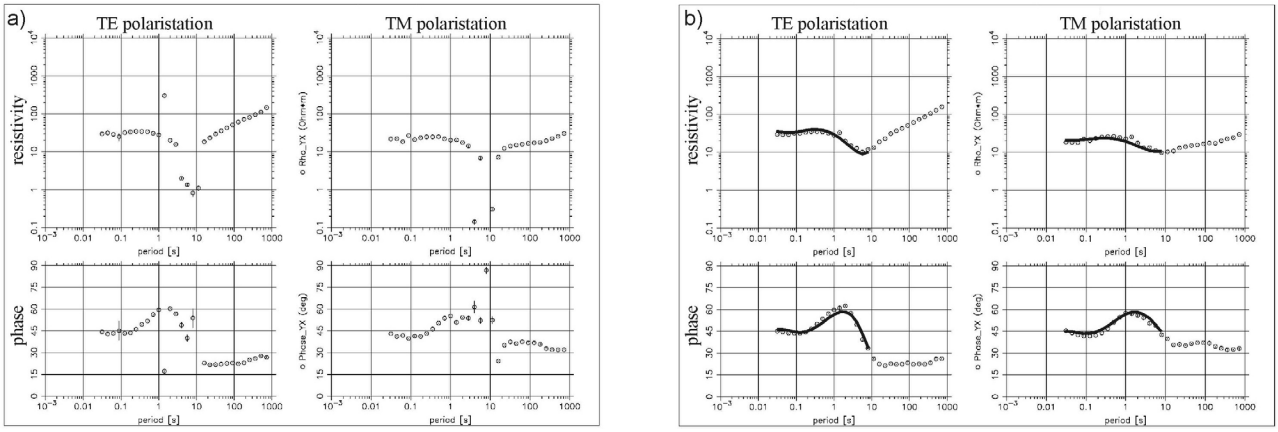

Figure 2. (a) Apparent resistivity and phase curves for a single site processed according to single-site technique. (b) The same site processed using noise separation [*Weckmann et al.*, 2005] and remote reference processing [*Krings*, 2007]. The model response is shown as a thick black line in the used period range.

and 3c show the strike direction distribution for both profile segments in a rose diagram. In comparison, the distribution for all sites and periods (Figure 3a) shows no clearly defined strike direction. Taking the magnetic declination of 3 degrees into account, the strike orientation is N61E in Israel (blue sites in Figure 1), and N11E (this is close to the alignment of the AF) in Jordan (green and red sites in Figure 1). The 90 degree uncertainty was solved by choosing the strike direction according to the general trend of the regional geological structures (such as the AF), which is also consistent with the direction of the induction arrows (not shown). With a changing geoelectric strike direction it was necessary to project the data onto a crooked profile (Figure 1). The directions of the two sections reflect a compromise between the calculated strike direction and the general orientation of the profiles along which the stations were deployed. Synthetic tests were performed to ensure this approach does not generate artificial anomalies (Text S1).[1]

2.3. The 2-D Inversion

[9] After being projected onto the profile and rotated to the appropriate angle, the data were ready for a 2-D inversion scheme. The WinGLink software package, which incorporates the RLM2DI algorithm [*Rodi and Mackie*, 2001] was used. The inversion was performed on a grid consisting of 93 rows and 274 columns. Both polarizations (TE and TM), as well as the vertical magnetic field were incorporated in the inversion. The inversion code of *Rodi and Mackie* [2001] uses a regularization parameter τ to control the trade-off between data misfit and model roughness. Following a series of inversions with different τ values, and examination of the resulting L curve between data misfit and model norm [*Parker*, 1994], a regularization parameter of $\tau = 10$ was deemed appropriate. Using a homogeneous half-space (taking the topography into account) with a resistivity of 100 Ωm as a starting model and error floors of 100% for TE apparent resistivity (to account for static shift), 10% for TM apparent resistivity, 1.5° for the phases and 0.05 for the vertical magnetic transfer functions, the inversion converged to a solution with the normalized RMS misfit of 1.31. Examples of the model fit are shown in Figure 2b.

[10] The resulting model is shown in Figure 4a. For the shallowest part the inversion model reveals a noncontinuous high conductivity layer (c1) extending along the northwestern half of the profile. This layer presents some local interruptions and reaches down to a few hundred meters below surface at its deepest point (between km 40 and 50). In particular the layer changes abruptly its depth coinciding with the surface trace of the AF (km 55). On the Jordan side, a continuous high conductivity layer is revealed at shallow depths (c2) extending along the southeastern half of the profile, under the Jordan highlands. However, the most prominent conductive feature of the model is a highly conductive half layer of varying depth and thickness located west of the AF (c3). The half layer starts at a depth of about 1 km below sea level reaches a maximum depth of 4300 m west of the AF. A small, localized conductive anomaly (c4) is located east of the AF, separated from the conductive half layer c3 and starting at a depth of approximately 2 km. The

[1]Auxiliary material files are available with the full article. doi:10.1029/2011GC003678.

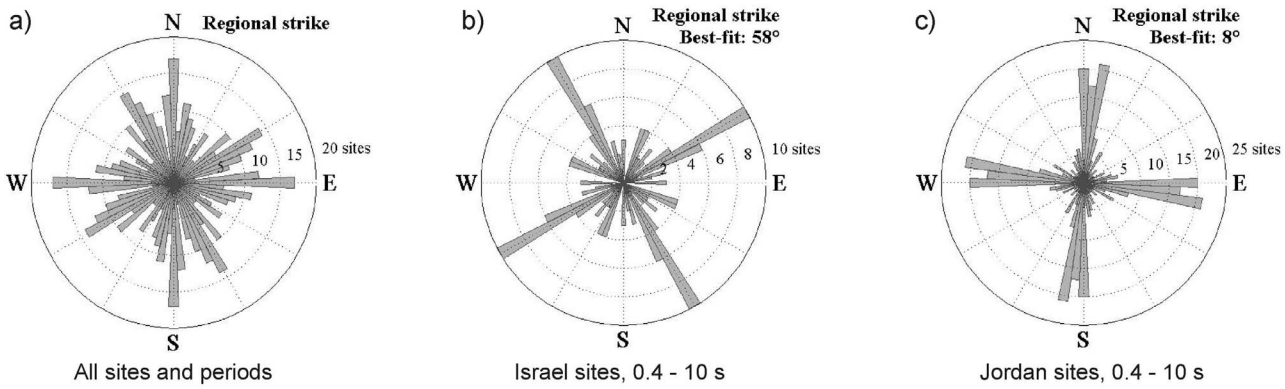

Figure 3. (a) Rose diagram of the strike directions calculated for each available site using the entire period range (0.03–1000 s). The distribution suggests that more than one strike direction is present. These become clear when sites on either side of the border ((b) Israel and (c) Jordan) are separated using the period range of 0.4–10 s.

southeastern half of the model is dominated by low conductivities (r1) starting approximately at sea level and extending down to more than 5 km. The model has been truncated at a depth of 5 km, which corresponds approximately to the sounding depth range of the used frequency range (up to 10 s) for the most conductive sections of the profile. *Ritter et al.* [2003] reported similar conductivity features from the inversion of the central part of the profile. The high conductivity half layer west of the AF was interpreted as related to brine filled Phanerozoic sediments, with the AF probably acting as a barrier to fluid circulation and thus keeping the fluids trapped west of it.

[11] Some sensitivity tests have been performed in order to test how well resolved are the different

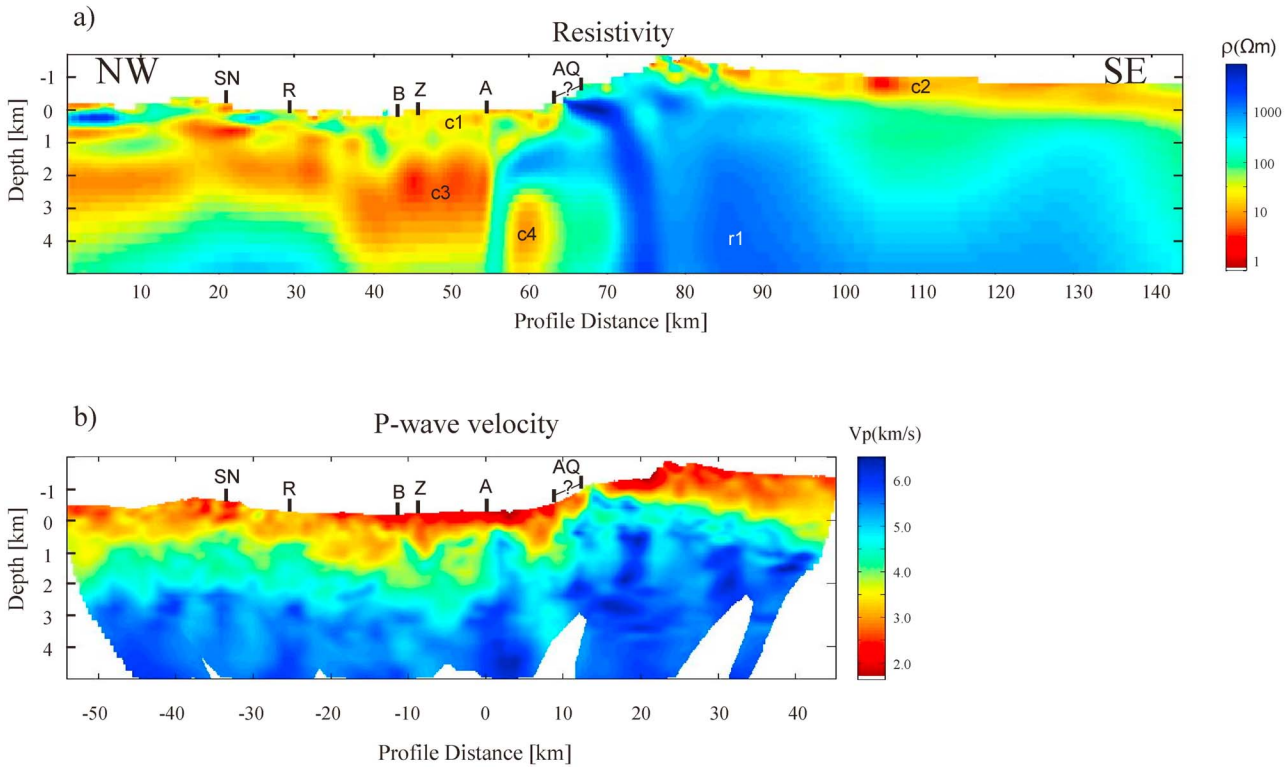

Figure 4. (a) The resistivity model computed in this study. The northwestern section of the profile is dominated by highly conductive structures. The Jordan highlands to the southeast exhibit a shallow (up to 1 km) conductive layer, beneath which highly resistive structures are seen. (b) P wave velocity model modified from *Ryberg et al.* [2007]. White regions beneath the surface indicate no ray coverage. Vertical exaggeration of 10:1 used for both models.

structures. A sensitivity test of a particular conductivity structure consists on modifying the structure being tested, e.g., changing the thickness of the conductive half layer c3, and computing the forward response of the modified model. By observing which frequencies and stations are mostly affected by these changes in the model we can get an idea of how well do the data control the modified parts of the model space. By subsequent reinversion of the data using the modified models as the starting model we can eventually obtain equivalent models in the sense that changes in the conductivity structure do not severely affect the data fit. In particular we tested whether the conductive layers c1 and c3 are separated by a higher resistivity zone, the thickness of the conductive layers c2 and c3 and the presence of the anomaly c4 and its possible connection with c3. The test suggest that the model is robust and the conductivity structures are required by the data. As a result of these sensitivity tests we conclude that c3 is separated both from c1 and c4 by zones of higher resistivity. The thicknesses of layers c2 and c3 shown in Figure 4a represent minimum values.

3. Joint Analysis of MT and Seismic Models

[12] In the framework of the DESERT project [*Weber et al.*, 2009], a number of seismic experiments were carried out in the area. Among these was a reflection seismic profile partially coincident with the MT profile [*Ryberg et al.*, 2007] (Figure 1). Tomographic inversion of shot-induced direct P wave arrivals was done to produce a P wave velocity model [*Ryberg et al.*, 2007] – this model is shown in Figure 4b. Velocities computed in this model can be resolved to depths of 5 km below sea level for most of the profile. This coincides with the resolvable depth of the resistivity model presented above, therefore this is the maximum depth considered in the joint interpretation of the two models.

3.1. Background

[13] Effectively combining seismic and magnetotelluric data sets remains a challenge in geophysics. While a number of algorithms for jointly inverting the data have been put forward [e.g., *Moorkamp et al.*, 2007; *Paasche and Tronicke*, 2007; *Gallardo and Meju*, 2011] these usually put geometrical constraints on the models, or assume a link between resistivity, ρ, and P wave velocity, v. As there is no fundamental law linking ρ, and v, and empirical relations between these parameters can hold locally within a specific lithology, here we follow the approach of *Bedrosian et al.* [2007] to lithological/geological structure classification using independent geophysical models.

[14] The first step in the approach is to align the two models with respect to each other, and to interpolate them onto a common grid. A set of colocated values for P wave velocity and resistivity are thus obtained, along with the relative uncertainties in each parameter (computed from ray hit count density from the seismic model, and the sensitivity map of the MT model), each pair of physical property values can then be seen as an outcome of a process defined by a probability density function (pdf). A complete pdf describes the full distribution and is computed by summing the pdf at each data point [*Schalkoff*, 1992]. As the resistivity spans several orders of magnitude, we use the logarithm of resistivity throughout our calculation:

$$pdf(\rho, v) = \frac{1}{n}\sum_{i=1}^{n} pdf_i(\rho, v) \tag{1}$$

where

$$pdf_i(\rho, v) = \frac{1}{\sqrt{2\pi}\delta\log(\rho_i)\delta v_i} e^{-\frac{1}{2}\left[\frac{(\log(\rho)-\log(\rho_i))^2}{\delta\log(\rho_i)^2} + \frac{(v-v_i)^2}{\delta v_i^2}\right]} \tag{2}$$

A high value of the pdf corresponds to a high probability of the given set of geophysical parameters coexisting in the interpolated grid. Assuming that lithological units are spatially connected, it would be possible to identify them as high-probability clusters in the pdf. A given number of classes can be identified, either manually picked, or calculated by fitting bivariate Gaussian functions to the pdf. Remapping the grid points constituting the identified clusters into the spatial domain can confirm if they indeed correspond to real continuous lithologies.

3.2. Interpolation of Models

[15] The first step in the joint interpretation of the two models is interpolating them onto a common grid. Due to the diffuse nature of electromagnetic fields the mesh used for the resistivity model becomes coarser with increasing depth, as well as being finer beneath the sections of the profile with denser site spacing. The velocity model is constructed on a regular grid, making all parts equally represented. Furthermore, the velocity model contains more data points than the resistivity model,

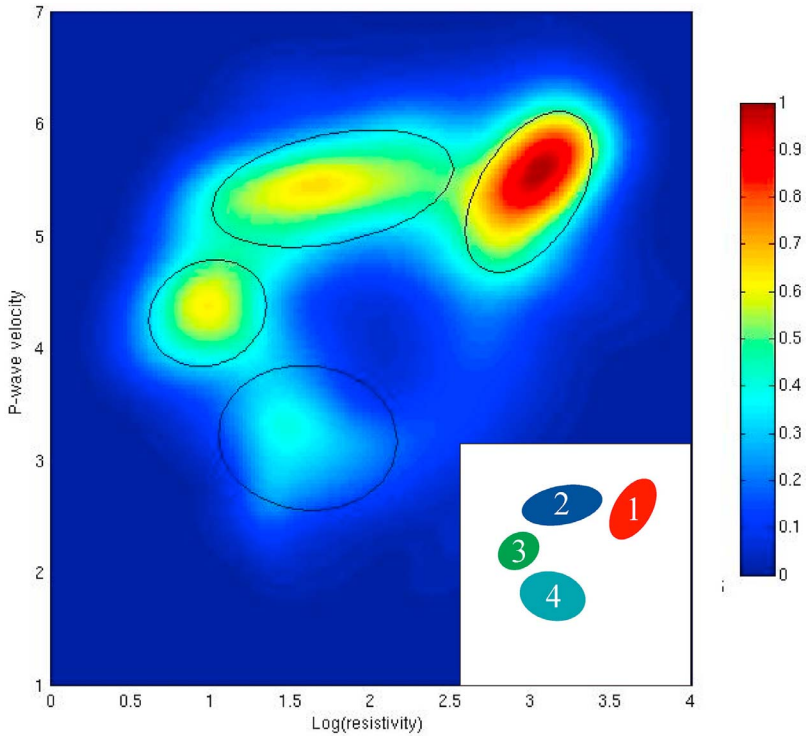

Figure 5. Probability density function computed using the appropriate interpolation parameters. The four clusters are indicated by their covariance ellipses. The inset shows the colors and numbers assigned to the clusters for discussion.

thus to avoid a loss of information we interpolate the resistivity model onto the velocity model.

[16] Such an interpolation requires a single resistivity value to be provided at each grid point of the velocity model. The inverse distance weighted (IDW) interpolation scheme, which estimates the weighted average of samples existing in the area within a specified buffer distance of the grid point, was used here. This interpolation scheme has been successfully used to jointly interpret velocity and resistivity models [e.g., *Muñoz et al.*, 2010]. The buffer size should be carefully chosen to avoid losing information contained in the resistivity model. When it is too small, some resistivity values will be too far away from any grid points, and will be ignored. On the other hand, a buffer too large will average a large number of points, leading to losing fine details and distorting sharp boundaries. The buffer should also not be constant, but increase with depth to accommodate the increasing sparseness of resistivity model grid points. The only reliable method to find the right buffer size is trial and error – various permutations need to be tried, and the stability of each solution must be tested. Examples of these are presented in Text S2. We conclude that buffer sizes varying from 0.2 to 0.4 km, with one resistivity value in the area defined by the buffer considered sufficient, are appropriate for our data. The pdf resulting from these parameters, with four prominent clusters, is shown in Figure 5.

[17] *Bedrosian et al.* [2007] developed the technique used here to identify local lithological classes – the profiles used in their study were 10 km long, and the technique has never been used for profiles 100 km long, as presented here. A potential problem with attempting to construct the pdfs using too much data is that where too many lithological classes are sampled, regions of high probability will become smeared due to overlapping parameter values from distinct classes. Furthermore, a lithology which exhibits particular geophysical parameters, but makes up a very slight portion of the profile space could have its high probability cluster covered by the flanks of more prominent classes. The maximum profile length to which the technique can be applied will depend on the number and type of lithologies the profiles cross. To satisfy ourselves that we can proceed with cluster identification from Figure 5, interpolations of various profile segments not longer than 30 km long were performed. The resulting pdfs always contained a selection of the clusters in Figure 5. When a short segment centered at the

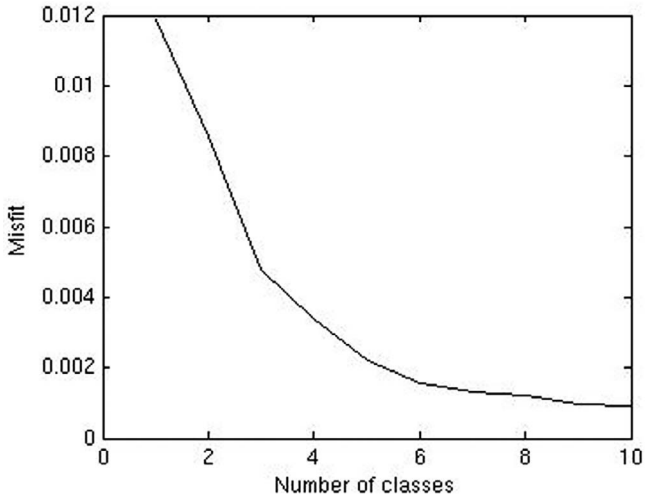

Figure 6. The L curve showing how the misfit between the calculated pdf and a simulation of an increasing number of bivariate Gaussian peaks decreases. The corner point is found around 4 or 5 classes, which represents the number of lithological classes likely to be resolved.

Arava Fault was analyzed, some clusters could be subdivided into two separate ones. These results agreed very well with the pdf presented in the 10 km analysis of *Bedrosian et al.* [2007]. We therefore conclude that proceeding with the classification will produce a reliable lithology distribution map beneath the entire profile. We acknowledge that in presenting a bigger picture some resolution will be lost in the region of the Arava Fault, and refer the reader to the previous study by *Bedrosian et al.* [2007] focusing on that particular zone.

3.3. Classification

[18] An important aspect of identifying clusters in a probability density function is the number of clusters to look for. While it is desirable to utilize all information contained in the models, it is important to avoid attempts at interpreting numerical artifacts. Representing each cluster as a bivariate Gaussian function, the least squares optimization technique of *Bedrosian et al.* [2007] is used to find the closest fit to the original pdf. The misfit between the two plotted as a function of the number of clusters used in the simulation will render a so-called L curve [e.g., *Parker*, 1994]. While every new Gaussian function used will decrease the misfit, after a certain point these improvements will become insignificant. The point of the maximum curvature of the L curve corresponds to the optimal number of classes. The misfit curve for the pdf in Figure 5 is shown in Figure 6. The curvature is consistent with the four clusters visible in the pdf, though the presence of a fifth class cannot be excluded.

[19] The next step in the analysis is identification of the clusters. The contour tracing half the amplitude of the maximum of a bivariate Gaussian function forms an ellipse, sometimes called the covariance ellipse [e.g., *Brandt*, 1999]. Thus cluster identification is performed manually, by constructing ellipses around the prominent clusters. While several clusters can be identified, one of them is much more prominent than the others, obscuring the geometry of the other ones. We therefore use an iterative approach, where after a cluster has been picked, a Gaussian function calculated from the cluster's position and width is subtracted from the pdf, making the remaining clusters more prominent. Figure 7 shows the progression. In Figure 7a the original pdf is seen. In Figure 7b, a white ellipse shows where the prominent cluster has been picked, and the pdf redrawn, scaled to its new highest value. This process is repeated for four clusters. Figure 7f shows how the amplitude of the pdf decreases with each cluster subtracted.

[20] The cluster locations and sizes picked are then used as the starting model for the automatic identification of clusters. Representing clusters as bivariate Gaussian functions, the manually identified clusters are adjusted to best fit the pdf (this technique is the same as was used for the L curve computation). Class boundaries are defined by the covariance ellipses, which contain ~60% of the respective class. The optimal clusters are shown in Figure 5, with their respective numbers by which they will from now on be referred to in the inset. Mapping these clusters in the profile space is shown in

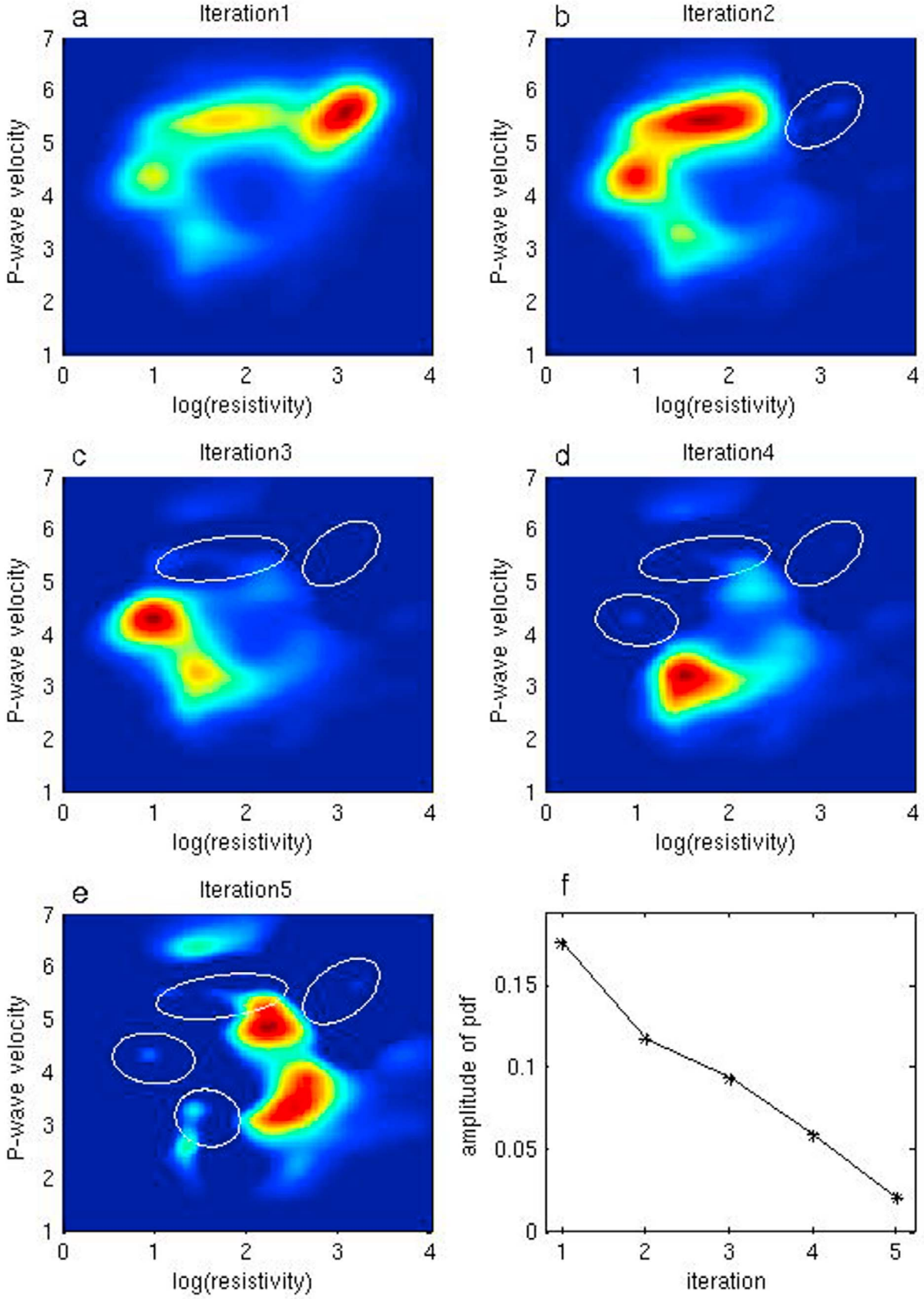
a
Iteration1
b
Iteration2
c
Iteration3
d
Iteration4
e
Iteration5
f
P-wave velocity
log(resistivity)
amplitude of pdf
iteration

Figure 7

Figure 8. The first and second panels show the P wave velocity and resistivity models, respectively. The third panel shows the spatial distribution of the best fit classes. These are mostly continuous, suggesting they do indeed correspond to real lithological structures. Location of surface exposures of major faults in the region has been indicated after *Sneh et al.* [1998]. The location of the Al Quweira Fault cannot be pinpointed, as the sites approximately follow its exposure for ~5 km. Such curves in station geometry are not optimal for a 2-D interpretation, and any model features directly beneath them must be interpreted with caution.

[21] While the automatic identification of clusters is dependent of the starting model (clusters picked manually), we found the solution presented in Figures 5 and 8 to be stable – the location of the four best fit clusters in parameter and spatial domains is independent of the starting model. Even when the original picks were deliberately incorrect (like picking only a fraction of a cluster, or a region slightly next to it), the best fit solution, and the remapped sections, looked similar to the ones presented. Furthermore, when the interpolation of the resistivity model onto the velocity model was performed using different parameters, as long as four clusters were present in the pdf, even if they were distorted, the remapped section did not differ significantly from the one in Figure 8.

[22] The L curve analysis (Figure 6) suggested that a fifth class might be present in the pdf. While the three clusters centered at velocities higher than 4 km/s all have elliptical shapes, the low-velocity cluster (Figure 7, iteration 4) has a more composite shape. It is therefore likely that if a fifth class does exist, it is this cluster (4) which needs to be separated into two. A starting model consisting of five classes was used to find the optimal solution, but the fifth class was found to heavily overlap with other classes. Different starting models were attempted, with various locations for the fifth class, but the solution never converged to a physically acceptable one. We therefore conclude that four lithological classes can be identified from the joint interpretation of velocity and resistivity models. Their distribution in parameter domain is shown in Figure 5, and in spatial domain in Figure 8.

4. Interpretation and Discussion

[23] A joint analysis of seismic and magnetotelluric models enabled us to identify four distinct lithological classes in the study area. Schematic interpretation is shown in the fourth panel of Figure 8. Class 4, illustrated in cyan in Figures 5 and 8, occupies the near surface, down to a maximum depth of 2 km, and is never overlain by another class. It is characterized by P wave velocities between 2.6 and 3.8 km/s and resistivities between 10 and 150 Ωm. As discussed previously by *Ryberg et al.* [2007] and based on the work by *Sneh et al.* [1998], these values are characteristic of Cretaceous and Paleogene sediments found throughout the region. These sediments are not found on the northwestern flanks of the Jordan highlands, which corresponds to the gap we observe in remapping the class between profile km +10 and +20 in the third panel of Figure 8.

[24] Class 3, presented in green, is found between depths of 1 and 3 km, underlying class 4. It exists only northwest of the Arava Fault, at which it abruptly terminates. It is characterized by P wave velocities between 3.9 and 4.9 km/s, and very low resistivity values, between 3 and 20 Ωm. The presence of this highly conductive body has already been observed during the analysis of the short MT profile carried out in 2000 [*Ritter et al.*, 2003; *Maercklin et al.*, 2005; *Bedrosian et al.*, 2007]. In the Zofar-20 well west of the AF saline waters were found at a depth of ~1000 m [*Ritter et al.*, 2003, and references therein]. These studies thus attributed the high conductivity to saline waters in the Permian and Triassic beds underlying the sediments described earlier, with the Arava Fault acting as an impermeable barrier to these fluids. This structure is unusual for active fault zones, which typically exhibit a zone of very high conductivity or low velocity associated with the fault zone. MT studies of the San Andreas fault found such a conductive zone ~1 km across and 1–2 km deep [*Unsworth et al.*, 2000; *Becken et al.*, 2008]. A study of trapped seismic waves along the

Figure 7. Identifying clusters from the pdf. (a) The first iteration shows the original pdf from Figure 5, and the most prominent cluster is picked. (b) In the next iteration this cluster has been removed by subtracting a Gaussian function with amplitude and width corresponding to the cluster; the covariance ellipse of this function is marked in white. The pdf has been rescaled to its highest remaining point in order to make the remaining clusters more clear. (b–e) This process is repeated for 4 clusters. The most prominent cluster seen at iteration 5 (after the 4th cluster was removed) is likely to represent residuals from the two most prominent clusters, and not a cluster corresponding to a separate class. (f) Plot showing the amplitude of the highest remaining point of the pdf at each iteration.

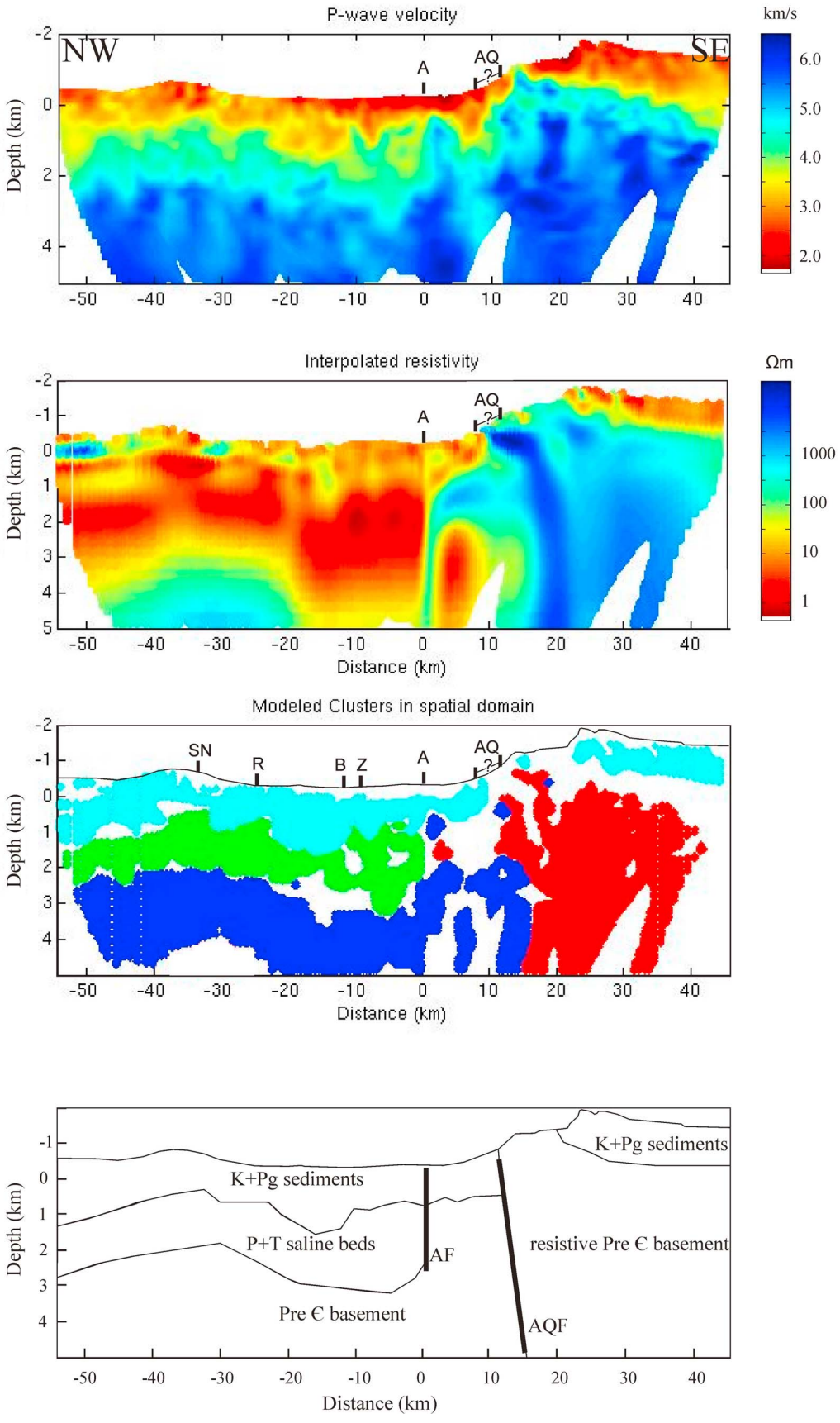
P-wave velocity
km/s
NW
SE
A
AQ
?
Depth (km)
6.0
5.0
4.0
3.0
2.0
Interpolated resistivity
Ωm
1000
100
10
1
Distance (km)
Modeled Clusters in spatial domain
SN
R
B
Z
K+Pg sediments
P+T saline beds
Pre Є basement
AF
AQF
resistive Pre Є basement

Figure 8

North Anatolian Fault derived fault zone widths of ~100 m [*Ben-Zion et al.*, 2003], while a similar study along the AF [*Haberland et al.*, 2003] found the fault zone to be 3–12 m wide, much too small to be resolved by the tomographic and MT models presented here.

[25] While our results confirm that the Arava Fault marks a sharp lithological boundary, this is only true down to a depth of ~3 km. The lithological class 2, presented here in blue, which underlies the highly conductive class 3 described previously, is observed on both sides of the Arava Fault. This class and class 1, presented in red, have very similar P wave velocities (~5–6 km/s), and therefore could not be differentiated with seismic tomography alone (Figures 4b and 8). The spatial distribution of both classes corresponds to the Precambrian basement inferred from boreholes [*Gilboa et al.*, 1993], geological mapping [*Sneh et al.*, 1998] and geophysics [*Weber et al.*, 2004; *Mechie et al.*, 2005; *Ryberg et al.*, 2007]. The classes, however, exhibit very different resistivities: 10–250 Ωm for class 2 (blue), and 300–2500 Ωm for class 1 (red), with the centers of the ellipses defining the classes in Figure 5 more than an order of magnitude apart.

[26] Modeling results guided by geological evidence [e.g., *Agnon and Eidelmann*, 1991; *Sobolev et al.*, 2005] suggest that at the beginning of transform motion deformation occurred in a rather wide belt with the reactivation of older N–S striking structures. Since the AF accommodates at most 60 km of lateral displacement [*Kesten et al.*, 2008, and references therein], a considerable amount of sinistral motion occurred along other faults during this phase. This horizontal movement was also associated by vertical motion, similar to other large faults like the San Andreas Fault Zone in the San Francisco Bay region, the Alpine Fault in New Zealand, the Queen Charlotte Fault in Canada, the Great Sumatran Fault in Indonesia, and the Tan-Lu Fault offshore China (*Aydin and Page* [1984], *Barnes et al.* [2001], *Rohr and Dietrich* [1992], *Bellier et al*. [1997], and *Hsiao et al*. [2004], respectively). This vertical movement can occur due to interaction of en echelon strike-slip faults [e.g., *ten Brink et al.*, 1996; *Dooley and McClay*, 1997]. There exists evidence for asymmetric Cenozoic uplift in the region [e.g., *Steinitz and Bartov*, 1991], with gravity modeling suggesting the eastern basement block has been lifted by 1.5 km more than the western block [*Tašárová et al.*, 2006]. This is also consistent with the basement depth map presented by *Stern and Johnson* [2010], which shows a significant shallowing (1–2 km) of depth to the basement toward south for the Arabian Plate over a distance of approximately 100 km. The significantly more resistive section of the Precambrian basement in the southeast could then represent a deeper section, which was uplifted further south in the Cenozoic, and was then transported north with the motion along the Dead Sea Transform. Furthermore, heating of the Arabian Plate resulted in it being uplifted by 1–1.5 km more than the African Plate [*Sobolev et al.*, 2005]. These two processes would account for relative uplift of 2–3 km, which is consistent with the difference in the minimum depth of classes 1 and 2 presented here (Figure 8). The contact between these classes is near the location of the Al Quweira Fault, the location of which cannot be exactly indicated due to a kink in site distribution following the fault for ~5 km, and then being projected onto the profile. If the contact is indeed at the Al Quweira Fault, the presence of the older, uplifted rocks east of it and the younger shallow basement west of it would suggest the sinistral motion took place along it, which would require it to be one of the principal active faults in the region immediately after the Cenozoic uplift, together with the Arava Fault. That the Al Quweira Fault might have played a more prominent role in the displacement between African and Arabian plates has already been proposed by using indirect evidence and a combination of seismics and satellite images [*Kesten et al.*, 2008], while a 40 km left-lateral offset at the Fault has been deduced from surface geology [*Barjous and Mikbel*, 1990]. Here we show again, that seismics alone would not have been able to separate the red and blue clusters of the Precambrian basement of Figure 8, but that only the combination of seismics and MT can differentiate the classes due to their different resistivities.

5. Conclusions

[27] We present the first comprehensive resistivity model from the 150 km magnetotelluric profile

Figure 8. Clusters from Figure 5 remapped in model space. The first panel shows the velocity model from Figure 4. The second panel shows the resistivity model interpolated onto the velocity model grid. The gaps in the model at depths greater than 3 km are due to ray coverage gaps in the velocity model. The third panel shows how the clusters remap into model space. Colors correspond to the inset of Figure 5. Surface locations of major faults crossed by the profile have been indicated: SN, Sa'ad Naafha; R, Ramon; B, Baraq; Z, Zofar; A, Arava; AQ, Al Quweira. Regions which did not fit into any clusters are white. The fourth panel shows the schematic stratigraphic interpretation.

carried out in the framework of the DESERT project across the Dead Sea Transform. The depth resolution of the model was ~5 km, which coincided with the resolution of a P wave velocity model computed during a coincident seismic experiment.

[28] A lithology structure classification was performed using a quantitative statistical approach based on the joint interpretation of the resistivity model with the aforementioned P wave velocity model. The approach assumes that continuous lithological structures can be distinguished according to specific values of geophysical parameters, in this case resistivity and P wave seismic velocity. After the two independent geophysical models have been interpolated onto a common grid, the pair of parameter values at each grid point, with their associated uncertainties, is projected into the probability density function in parameter space. Regions of enhanced probability, or classes, can then be remapped into spatial domain, where if these correspond to topologically continuous features, it is assumed the classes correspond to real lithological units exhibiting geophysical parameters characterizing the class.

[29] Four classes were identified in parameter space, which were all remapped as lithological units. It was shown that a higher number of classes cannot be accommodated by the models when they are considered in their entirety. One class was interpreted as Cretaceous and Paleogene sediments found throughout the study area down to a depth of ~1 km. Another was a highly conductive body at depths between 1 and 3 km on the northwest side of, and terminating at, the Arava Fault. This is consistent with previous studies which suggested high saline content in the Permian and Triassic deposits, with the Arava Fault acting as a barrier to fluid flow. While there exist a number of large faults in the upper crust west of the AF, none of them exhibits a zone of decreased P wave velocity or high conductivity typical for damage zones. The remaining two classes subdivide the Precambrian basement, with a much more resistive section east of the Al Quweira Fault possibly uplifted in relation to the western section, and transported northward due to the plate motion along the DST. The AF is the main active fault of the DST, but has accommodated not more than 60 km of the overall plate motion [*Kesten et al.*, 2008, and references therein]. We thus propose that the Al Quweira Fault was previously active, and deformation along the DST began along it, before being shifted to the AF.

Acknowledgments

[30] The DESERT project was funded by the Deutsche Forschungsgemeinschaft. The National Ministry of Infrastructure of Israel, the Natural Resources Authority of Jordan, and the An-Najan National University in Nablus, Palestine, are thanked for their support. The instruments were provided by the Geophysical Instrument Pool Potsdam (GIPP). We gratefully acknowledge the work of all the field crews. J.S. is funded by the Helmholtz-Russia Joint Research Groups (Project HRJRG-110). P.A.B. was supported by the Alexander von Humboldt Foundation. Robert J. Stern and anonymous reviewers provided constructive feedback on earlier versions of the article.

References

Abu Taimeh, A. (1988), Structural and applied remote sensing studies at Gharandal-Petra area, eastern Wadi Araba, M.Sc. thesis, Univ. of Jordan, Amman, Jordan.

Agnon, A., and A. Eidelmann (1991), Lithospheric breakup in three dimensions: Necking of a work-hardening plastic plate, *J. Geophys. Res.*, *96*, 20,189–20,194, doi:10.1029/91JB01888.

Aldersons, F., Z. Ben-Avraham, A. Hofstetter, E. Kissling, and T. Al-Yazjeen (2003), Lower-crustal strength under the Dead Sea basin from local earthquake data and rheological modeling, *Earth Planet. Sci. Lett.*, *214*, 129–142, doi:10.1016/S0012-821X(03)00381-9.

Aydin, A., and R. A. Page (1984), Diverse Pliocene-Quaternary tectonics in a transform environment, San Francisco Bay region, California, *Geol. Soc. Am. Bull.*, *95*, 1303–1317, doi:10.1130/0016-7606(1984)95<1303:DPTIAT>2.0.CO;2.

Barjous, M. O. (1988), Structural study of the area between Petra and Ash Shawbak, M.Sc. thesis, Univ. of Jordan, Amman, Jordan.

Barjous, M., and S. Mikbel (1990), Tectonic evolution of the Gulf of Aqaba–Dead Sea transform fault system, *Tectonophysics*, *180*, 49–59, doi:10.1016/0040-1951(90)90371-E.

Barnes, P. M., R. Sutherland, B. Davy, and J. Delteil (2001), Rapid creation and destruction of sedimentary basins on mature strike-slip faults: An example from the off-shore Alpine Fault, New Zealand, *J. Struct. Geol.*, *23*, 1727–1739, doi:10.1016/S0191-8141(01)00044-X.

Becken, M., and H. Burkhardt (2004), An ellipticity criterion in magnetotelluric tensor analysis, *Geophys. J. Int.*, *159*, 69–82, doi:10.1111/j.1365-246X.2004.02376.x.

Becken, M., O. Ritter, S. K. Park, P. A. Bedrosian, U. Weckmann, and M. Weber (2008), A deep crustal fluid channel into the San Andreas Fault system near Parkfield, California, *Geophys. J. Int.*, *173*, 718–732, doi:10.1111/j.1365-246X.2008.03754.x.

Bedrosian, P., N. Maercklin, U. Weckmann, Y. Bartov, T. Ryberg, and O. Ritter (2007), Lithology-derived structure classification from the joint interpretation of magnetotelluric and seismic models, *Geophys. J. Int.*, *170*, 737–748, doi:10.1111/j.1365-246X.2007.03440.x.

Bellier, O., M. Sebrier, T. Pramumijoyo, T. Beaudouin, H. Harjono, I. Bahr, and O. Forni (1997), Paleoseismicity and seismic hazard along the Great Sumatran Fault (Indonesia), *J. Geodyn.*, *24*, 169–183, doi:10.1016/S0264-3707(96)00051-8.

Ben-Zion, Y., Z. Peng, D. Okaya, L. Seeber, J. G. Armbruster, N. Ozer, A. J. Michael, S. Baris, and M. Aktar (2003), A shallow fault-zone structure illuminated by trapped waves

in the Karadere-Duzca branch of the North Anatolian Fault, western Turkey, *Geophys. J. Int.*, *152*, 699–717, doi:10.1046/j.1365-246X.2003.01870.x.

Brandt, S. (1999), *Data Analysis: Statistical and Computational Methods for Scientists and Engineers*, 655 pp., Springer, New York.

DESERT Group (2000), Multinational geoscientific research effort kicks off in the Middle East, *Eos Trans. AGU*, *81*, 609.

Dooley, T., and K. McClay (1997), Analog modelling of pull-apart basins, *AAPG Bull.*, *81*(11), 1804–1826.

Ezersky, M. (2008), Geoelectric structure of the Ein Gedi sink-hole occurrence site at the Dead Sea shore in Israel, *J. Appl. Geophys.*, *64*, 56–69, doi:10.1016/j.jappgeo.2007.12.003.

Gallardo, L. A., and M. A. Meju (2011), Structure-coupled multiphysics imaging in geophysical sciences, *Rev. Geophys.*, *49*, RG1003, doi:10.1029/2010RG000330.

Gamble, T. D., W. M. Goubau, and J. Clarke (1979), Error analysis for remote reference magnetotellurics, *Geophysics*, *44*, 959–968, doi:10.1190/1.1440988.

Garfunkel, Z., and Z. Ben-Avraham (1996), The structure of the Dead Sea basin, *Tectonophysics*, *266*, 155–176, doi:10.1016/S0040-1951(96)00188-6.

Garfunkel, Z., I. Zak, and R. Freund (1981), Active faulting in the Dead Sea Rift, *Tectonophysics*, *80*, 1–26, doi:10.1016/0040-1951(81)90139-6.

Gilboa, Y., H. Fligelman, and B. Derin (1993), Zohar-Kidod-Haqanaim fields–Israel, Eastern Mediterranean Basin, in *Treatise of Petroleum Geology Atlas of Oil and Gas Fields*, edited by N. H. Foster and E. A. Beaumont, pp. 129–152, Am. Assoc. of Pet. Geol, Tulsa, Okla.

Haberland, C., A. Agnon, R. El-Kelani, N. Maercklin, I. Qabbani, G. Rümpker, T. Ryberg, F. Scherbaum, and M. Weber (2003), Modeling of seismic guided waves at the Dead Sea Transform, *J. Geophys. Res.*, *108*(B7), 2342, doi:10.1029/2002JB002309.

Hsiao, L. Y., S. A. Graham, and N. Tilander (2004), Seismic reflection imaging of a major strike-slip fault zone in a rift system: Paleogene structure and evolution of the Tan-Lu fault system, Liadong Bay, Bohai, offshore China, *AAPG Bull.*, *88*, 71–97, doi:10.1306/09090302019.

Kesten, D., M. Weber, C. Haberland, C. Janssen, A. Agnon, Y. Bartov, and I. Rabba, and the DESERT Group (2008), Combining satellite and seismic images to analyse the shallow structure of the Dead Sea Transform near the DESERT transect, *Int. J. Earth Sci.*, *97*, 153–169, doi:10.1007/s00531-006-0168-5.

Klinger, Y., L. Avouac, L. Dorbath, N. A. Karaki, and N. Tisnerat (2000), Seismic behaviour of the Dead Sea Fault along Araba valley, Jordan, *Geophys. J. Int.*, *142*, 769–782, doi:10.1046/j.1365-246x.2000.00166.x.

Krings, T. (2007), The influence of robust statistics, remote reference, and horizontal magnetic transfer functions on data processing in magnetotellurics, diploma thesis, Westfälische Wilhelms-Univ. Münster, Munster, Germany.

Maercklin, N., P. A. Bedrosian, C. Haberland, O. Ritter, T. Ryberg, and M. Weber (2005), Characterizing a large shear-zone with seismic and magnetotelluric methods: The case of the Dead Sea Transform, *Geophys. Res. Lett.*, *32*, L15303, doi:10.1029/2005GL022724.

Mechie, J., K. Abu-Ayyash, Z. Ben-Avraham, R. El-Kelani, A. Moshen, G. Rümpker, J. Saul, and M. Weber (2005), Crustal shear velocity structure across the Dead Sea Transform from two-dimensional modelling of DESERT project explosion seismic data, *Geophys. J. Int.*, *160*, 910–924, doi:10.1111/j.1365-246X.2005.02526.x.

Mohsen, A., R. Hofstetter, G. Bock, R. Kind, M. Weber, K. Wylegalla, G. Rümpker, and the DESERT Group, (2005), A receiver function study across the Dead Sea Transform, *Geophys. J. Int.*, *160*, 948–960, doi:10.1111/j.1365-246X.2005.02534.x.

Mohsen, A., R. Kind, S. Sobolev, and M. Weber, and the DESERT Group (2006), Thickness of the lithosphere east of the Dead Sea Transform, *Geophys. J. Int.*, *167*, 845–852, doi:10.1111/j.1365-246X.2006.03185.x.

Moorkamp, M., A. G. Jones, and D. W. Eaton (2007), Joint inversion of teleseismic receiver functions and magnetotelluric data using a genetic algorithm: Are seismic velocities and electrical conductivities compatible, *Geophys. Res. Lett.*, *34*, L16311, doi:10.1029/2007GL030519.

Muñoz, G., K. Bauer, I. Moeck, A. Schulze, and O. Ritter (2010), Exploring the Gross Schoenebeck (Germany) geothermal site using statistical joint interpretation of magnetotelluric and seismic tomography models, *Geothermics*, *39*, 35–45, doi:10.1016/j.geothermics.2009.12.004.

Paasche, H., and J. Tronicke (2007), Cooperative inversion of 2D geophysical data sets: A zonal approach based on fuzzy c-means cluster analysis, *Geophysics*, *72*(3), A35–A39, doi:10.1190/1.2670341.

Parker, R. L. (1994), *Geophysical Inverse Theory*, 400 pp., Princeton Univ. Press, Princeton, N. J.

Quennell, A. M. (1958), The structural and geomorphic evolution of the Dead Sea rift, *Q. J. Geol. Soc. London*, *114*, 1–24, doi:10.1144/gsjgs.114.1.0001.

Ritter, O., A. Junge, and G. J. K. Dawes (1998), New equipment and processing for magnetotelluric remote reference observations, *Geophys. J. Int.*, *132*, 535–548, doi:10.1046/j.1365-246X.1998.00440.x.

Ritter, O., T. Ryberg, U. Weckmann, A. Hoffmann-Rothe, A. Abueladas, Z. Garfunkel, and DESERT Research Group, (2003), Geophysical images of the Dead Sea Transform in Jordan reveal an impermeable barrier for fluid flow, *Geophys. Res. Lett.*, *30*(14), 1741, doi:10.1029/2003GL017541.

Rödder, A. (2010), Interpretation von SHOTEM Daten mit mehrdimensionalen Leitfähigkeitsmodellen am Beispiel der Araba Verwerfung, Jordanien, Ph.D. thesis, Univ. of Köln, Cologne, Germany.

Rodi, W., and R. L. Mackie (2001), Nonlinear conjugate gradients algorithm for 2D magnetotelluric inversion, *Geophysics*, *66*, 174–181, doi:10.1190/1.1444893.

Rohr, K. M., and J. R. Dietrich (1992), Strike-slip tectonics and development of the Tertiary Queen Charlotte Basin, offshore western Canada: Evidence from seismic reflection data, *Basin Res.*, *4*, 1–20, doi:10.1111/j.1365-2117.1992.tb00039.x.

Rotstein, Y., and S. Goldberg (1981), Magnetotelluric profile across the Dead Sea Rift in northern Israel, *Tectonophysics*, *80*, 147–164, doi:10.1016/0040-1951(81)90147-5.

Ryberg, T., M. H. Weber, Z. Garfunkel, and Y. Bartov (2007), The shallow velocity structure across the Dead Sea Transform fault, Arava Valley, from seismic data, *J. Geophys. Res.*, *112*, B08307, doi:10.1029/2006JB004563.

Schalkoff, R. (1992), *Pattern Recognition: Statistical, Structural, and Neural Approaches*, 364 pp., John Wiley, New York.

Sneh, A., Y. Bartov, T. Weissbrod, and M. Rosensaft (1998), Geological map of Israel 1:200000, sheets 3 and 4, Geol. Surv. of Israel, Jerusalem.

Sobolev, S. V., A. Petrunin, Z. Garfunkel, and A. Y. Babeyko, and the DESERT Group (2005), Thermo-mechanical model of the Dead Sea Transform, *Earth Planet. Sci. Lett.*, *238*, 78–95, doi:10.1016/j.epsl.2005.06.058.

Steinitz, G., and Y. Bartov (1991), The Miocene-Pliocene history of the Dead Sea segment of the Rift in light of K-Ar ages of basalt, *Isr. J. Earth Sci.*, *40*, 199–208.

Stern, R. J., and P. Johnson (2010), Continental lithosphere of the Arabian Plate: A geologic, petrologic, and geophysical synthesis, *Earth Sci. Rev.*, *101*, 29–67, doi:10.1016/j.earscirev.2010.01.002.

Tašárová, Z., H. J. Götze, R. El-Kelani, J. Ebling, and M. Hassouneh (2006), Small-scale gravity modeling of upper-crustal structures in the Araba Valley along the Dead Sea Transform, *Geochem. Geophys. Geosyst.*, *7*, Q09012, doi:10.1029/2005GC001229.

ten Brink, U. S., Z. Ben-Avraham, R. E. Bell, M. Hassouneh, D. F. Coleman, G. Andersen, G. Tibor, and B. Coakley (1993), Structure of the Dead Sea pull-apart basin from gravity anomalies, *J. Geophys. Res.*, *98*(B12), 21,877–21,894, doi:10.1029/93JB02025.

ten Brink, U. S., R. Katzman, and J. Lin (1996), Three-dimensional models of deformation near strike-slip faults, *J. Geophys. Res.*, *101*, 16,205–16,220, doi:10.1029/96JB00877.

Unsworth, M., P. Bedrosian, M. Eisel, G. Egbert, and W. Siripunvaraporn (2000), Along strike variations in the electrical structure of the San Andreas Fault at Parkfield, California, *Geophys. Res. Lett.*, *27*(18), 3021–3024, doi:10.1029/2000GL011476.

Weber, M. H., et al. (2004), The crustal structure of the Dead Sea Transform, *Geophys. J. Int.*, *156*, 655–681, doi:10.1111/j.1365-246X.2004.02143.x.

Weber, M. H., et al. (2009), Anatomy of the Dead Sea Transform from lithospheric to microscopic scale, *Rev. Geophys.*, *47*, RG2002, doi:10.1029/2008RG000264.

Weckmann, U., A. Magunia, and O. Ritter (2005), Effective noise separation for magnetotelluric single site data processing using a frequency domain selection scheme, *Geophys. J. Int.*, *161*, 635–652, doi:10.1111/j.1365-246X.2005.02621.x.